

Fusion of sensor geometry into additive strain fields measured with sensing skin

Austin Downey^{1,2} , Mohammadkazem Sadoughi¹ ,
Simon Laflamme^{2,3}  and Chao Hu^{1,3} 

¹ Department of Mechanical Engineering, Iowa State University, Ames, IA, United States of America

² Department of Civil, Construction, and Environmental Engineering, Iowa State University, Ames, IA, United States of America

³ Department of Electrical and Computer Engineering, Iowa State University, Ames, IA, United States of America

E-mail: adowney2@iastate.edu

Received 28 March 2018, revised 7 May 2018

Accepted for publication 15 May 2018

Published 11 June 2018



CrossMark

Abstract

Recently, numerous studies have been conducted on flexible skin-like membranes for the cost effective monitoring of large-scale structures. The authors have proposed a large-area electronic consisting of a soft elastomeric capacitor (SEC) that transduces a structure's strain into a measurable change in capacitance. Arranged in a network configuration, SECs deployed onto the surface of a structure could be used to reconstruct strain maps. Several regression methods have been recently developed with the purpose of reconstructing such maps, but all these algorithms assumed that each SEC-measured strain located at its geometric center. This assumption may not be realistic since an SEC measures the average strain value of the whole area covered by the sensor. One solution is to reduce the size of each SEC, but this would also increase the number of required sensors needed to cover the large-scale structure, therefore increasing the need for the power and data acquisition capabilities. Instead, this study proposes an algorithm that accounts for the sensor's strain averaging feature by adjusting the strain measurements and constructing a full-field strain map using the kriging interpolation method. The proposed algorithm fuses the geometry of an SEC sensor into the strain map reconstruction in order to adaptively adjust the average kriging-estimated strain of the area monitored by the sensor to the signal. Results show that by considering the sensor geometry, in addition to the sensor signal and location, the proposed strain map adjustment algorithm is capable of producing more accurate full-field strain maps than the traditional spatial interpolation method that considered only signal and location.

Supplementary material for this article is available [online](#)

Keywords: structural health monitoring, capacitive-based sensor, soft elastomeric capacitor, flexible membrane sensor, additive strain maps, full-field strain maps, sensor fusion

(Some figures may appear in colour only in the online journal)

1. Introduction

Recent advances in sensor technologies have reduced the costs associated with the instrumentation of large-scale (or mesoscale) structures, including civil, aerospace, and energy structures, for structural health monitoring applications [1]. This reduction in cost enables the deployment of distributed dense sensor networks for direct damage sensing over large

surfaces. Direct sensing is generally considered to be one of the two categories of methods used for the detection and localization of damage, with the other category being the indirect methods [2]. Indirect sensing technologies (e.g. accelerometers) and methods involve the measurement of a structure's global condition through an often sparse array of sensors. However, the likelihood that a local damage will directly affect the signal output of a sensor is low. As a

consequence, these methods rely on sophisticated data analysis and damage detection algorithms. Indirect sensing technologies can be sensitive to, and their application limited by, noisy measurements, complex structures, and/or environmental variations (e.g. humidity and thermal) [3, 4]. In contrast, direct sensing methods involve the deployment of distributed dense sensor networks that are capable of directly inferring damage from a change in a signal with only simple, often called ‘threshold’ algorithms [5]. Examples of strain-based direct damage sensing technologies include fiber-optic sensors, vibrating wire, and resistive strain gauges (RSGs). To provide a structure with a high probability of detection for cracks and other strain field anomalies, a large number of individual sensors are required [2, 6–8]. While mature technologies such as fiber-optic sensors or vibrating wires can be spatially distributed to increase their damage detection resolution, their relatively high costs (including sensors, data acquisition (DAQ), and installation) and relative bulkiness [9] when mounted on the surface of a structure make them less suited for the monitoring of mesoscale structures [4, 10].

The need for spatially distributed strain sensing technologies has been recognized by multiple researchers and addressed using various techniques. One such technique is electrical impedance tomography (EIT) where either the electrical conductivity, permittivity, or impedance is inferred from the electrical measurements made on the surface of a structure. These measurements are then used to generate a tomographic image of the component. EIT has been used for damage detection in structures by measuring the electrical changes in carbon nanotube skins [11, 12], copper doped conductive paints [13, 14], or through the component itself [15]. While EIT is capable of producing a relatively high spatial resolution, it requires a high contact density and repeated measurements to solve the tomography mapping’s inverse problem. In addition, as the analytical solution for the inverse mapping problem is difficult (or sometimes impossible) to formulate, the finite element or finite difference method must be used to obtain an approximate solution [16]. Despite high spatial resolution capabilities, the requirements for repeated measurements using a variety of contacts and for solving the inverse mapping problem make the EIT technique not well suited for every application. Another electrical tomography technique uses a resistor mesh model to detect and localize damage-induced strain changes in cement doped with multi-walled carbon nanotubes [17]. However, this model-assisted approach requires that damage be located through the use of a searching method that updates the resistor mesh model associated with the structure, thus adding a relatively high computational cost to the approach [18]. Another notable method to collect spatially distributed strain data is the use of optical measurements (e.g. cameras and photocells) leveraging either digital image correlation [19] or photoactive nanocomposites that generate small amounts of light when various levels of strain are reached [20]. While these measurement systems benefit from their being non-contact methods, their requirement of having either a camera or photocell set back from the structure limits their deployment in some applications.

The use of large-area electronics or sensing skins for the condition assessment of structures is an emerging technology enabling a broad range of sensors and their associated electronics to be integrated onto a single sheet [21, 22]. These sensing skins allow for the easy installation of a high number of discrete sensors over a large-scale surface. The discrete sensors that make up a sensing skin allow for the direct detection and localization of damage. These sensing skins are analogous to biological skin in that they are capable of detecting and localizing damage over a structure’s global area. Various researchers have proposed sensing skins that are self-contained units, with all the sensing, DAQ, power harvesting, and communications built onto a single flexible sheet. Numerous examples of sensing skins, at various stages of development, have been tested at the laboratory scale. One example is a sensing skin that uses a plurality of traditional RSGs and integrated circuits mounted onto a single flexible substrate [23]. A prototype of this RSG based sensing skin was fabricated where communications between the sensors and integrated circuits were done through conductive and capacitive antennas to provide a low-cost and scalable architecture [24]. Other researchers have looked at using polymer materials doped with carbon nanotubes to form piezoresistive strain sensors [25–27] that could be combined with electronics to constitute sensing skins. One such example is a fully integrated sensing skin that combined thin-film resistive sensors fabricated from a carbon nanotube composite with the required electronics for on-board resistance measurements [28]. Other promising approaches for the realization of large-scale sensing skins include using a CO₂ laser to directly write RSGs onto a polyimide film to form graphitic porous sensor arrays that could be easily customizable in shape and size [29] and the use of strain sensors printed with conductive ink [30].

Another sensing skin, being developed by the authors of this paper, is based on a densely deployed network of low-cost large-area capacitor termed the soft elastomeric capacitor (SEC) [31]. The SEC is a robust and durable sensor [32] that is customizable in both shape and size. One particularly useful attribute of the SEC is its capability to measure the additive strain of a structure ($\epsilon_x + \epsilon_y$) [31]. The individual SEC has been characterized for both its static [33] and dynamic [34] behaviors. The sensing skin consisting of a network of SEC sensors has been used for the generation of full-field uni-directional strain maps [35, 36], and for the detection of fatigue cracks in steel bridges [37]. Additionally, an SEC-based sensing skin has been studied for the detection and localization of damage on a wind turbine blade, both numerically [38] and experimentally [39].

Because the SEC is a strain transducing sensor, it follows that a network of SECs deployed onto the surface of a structure could be used to reconstruct strain maps. An approximated full-field additive strain map can be reconstructed by assuming that the measurement of each SEC is located in the geometric center of the SEC and interpolating the measurement points between adjacent SECs. Various interpolation methods can be used for this task, including radial basis functions [40], cubic splines [41], and kriging (or

Gaussian process regression) [42]. As the number and density of SECs deployed over a given area increases, the approximated full-field strain map will become more accurate due to the capability of the SEC network to reproduce more complex strain topographies. However, as with any sensing technology, an increase in the number of sensors deployed onto a structure necessitates increased power, DAQ capabilities, and communication hardware. Therefore, a trade-off must be made between the cost (economic and technical) associated with a particular sensor density and the required strain map resolution. To help reduce the severity of this trade-off, this work introduces a robust algorithm that fuses the geometry (i.e. the area) of the SEC sensor into the previously discussed strain map interpolation method that relied solely on the sensor signal and sensor location.

The strain map adjustment algorithm works by first building a traditional full-field strain map using the SEC sensor signals and locations and then interpolating the measurement points between the sensors. In this work kriging is used as the interpolation method. Next, the sensor geometry is fused into the strain map by calculating what the signal of each SEC should be using the kriging-estimated strain map under the area covered by each sensor and adjusting the SEC signal used for training the kriging model. Thereafter, the computation iteratively adjusts the SEC signal used for training the kriging model until the estimated signal from the kriging-derived strain map converges to the actual signal of the SECs. The improvement in full-field strain estimation allows for more accurate damage and strain field anomaly detection. In cases where uni-directional strain maps are needed, this algorithm can be used to improve the accuracy of the additive strain field used in the decomposition task using a previously proposed kriging-based [35] or least squares-based [36] algorithm. Results show that by considering the sensor geometry, in addition to the sensor signal and location, the proposed strain map adjustment algorithm is capable of producing more accurate full-field strain maps with a given number of sensors than the traditional interpolation method that considered only the sensor signal and location.

2. Background

This section provides a brief review of the SEC sensor that forms the basis of the SEC-based sensing skin, followed by a brief introduction to the kriging method used in this work.

2.1. Soft elastomeric capacitor

The SEC is a highly scalable thin-film strain sensor. Figure 1 presents a square SEC with a area of 56 cm². The sensor is a parallel plate capacitor with its strain sensing principle derived from the fact that a change in area (i.e., strain) of the monitored structure will provoke a measurable change in its capacitance. The fabrication process of the SEC is simple and highly scalable, because it does not require any highly specialized manufacturing or processing equipment. The dielectric of the capacitor is constituted from an SEBS block co-

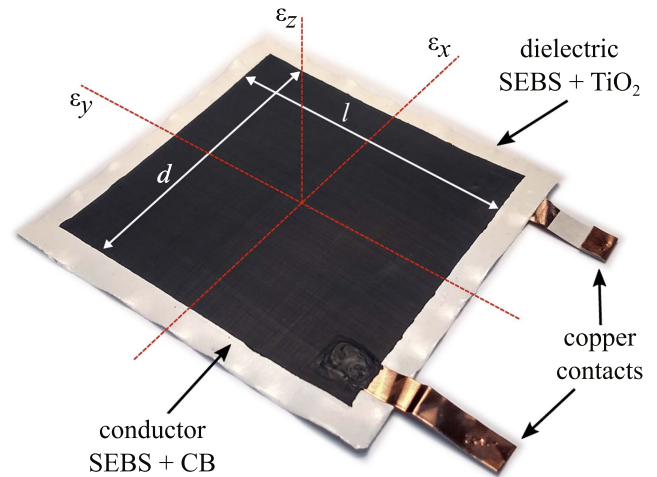


Figure 1. An SEC sensor with key components, dimensions, and axes annotated.

polymer filled with TiO₂ to increase both its durability [32, 43] and permittivity [44]. The conductive layers painted onto each side of the SEC sensor are fabricated by doping the same SEBS but filled carbon black instead of TiO₂. Carbon black is used as the conductive filler as it allows for conductive pathways to form within the SEBS matrix. Additionally, it absorbs both UV and visible light [45] and has demonstrated resiliency to weathering [32]. Currently, electrical connections are made to the painted conductive layers of the SEC using copper contacts. To ensure a good connection between the copper contact and SEBS-based conductive paint, a thin layer of the conductive paint is added on top of the copper contacts as denoted in figure 1. For more details regarding the manufacturing process of the SEC sensors, the interested reader is referred to [31, 34].

An electro-mechanical model that relates a change in area of the monitored structure to a measurable change in capacitance can be derived by taking the capacitance (C) of a parallel plate capacitor, modeled as a non-lossy parallel plate capacitor:

$$C = \epsilon_0 \epsilon_r \frac{A}{h}, \quad (1)$$

where $\epsilon_0 = 8.854 \text{ pF m}^{-1}$ is the vacuum permittivity, ϵ_r is the polymer's relative permittivity, $A = d \cdot l$ is the sensor area of width d and length l (as annotated in figure 1), and h is the thickness of the dielectric. Assuming small strains, equation (1) can be written as a change in capacitance (ΔC):

$$\frac{\Delta C}{C} = \frac{\Delta d}{d} + \frac{\Delta l}{l} - \frac{\Delta h}{h}, \quad (2)$$

where it can be noted that $\Delta d/d$, $\Delta l/l$, and $\Delta h/h$, can be expressed as strain components ϵ_x , ϵ_y , and ϵ_z , respectively. Assuming a plane stress condition, $\epsilon_z = -\nu/(1 - \nu) \cdot (\epsilon_x + \epsilon_y)$, a relative change in capacitance ΔC can be related to a change in the sensor's deformation as:

$$\frac{\Delta C}{C} = \lambda(\epsilon_x + \epsilon_y), \quad (3)$$

where ν is the sensor material's Poisson's ratio taken as $\nu \approx 0.49$ [46]. Therefore, $\lambda = 1/(1 - \nu) \approx 2$ represents the

gauge factor of the sensor. A key advantage of the SEC is its capability to measure the additive strain of a structure, as shown in equation (3).

Algorithm 1. Pseudocode for the strain map adjustment algorithm

-
- 1: Build and run the initial kriging model.
 - 2: Use the kriging model to calculate the estimated SEC signal.
 - 3: Calculate the difference between the SEC signal and the kriging model's estimated SEC signal.
 - 4: **while** difference > difference threshold **do**:
 - 5: Add the difference to the SEC signal.
 - 6: Build and run the updated kriging model.
 - 7: Use the updated kriging model to calculate the estimated SEC signal.
 - 8: Calculate the difference between the SEC signal and the kriging model's estimated strain.
 - 9: **end while**
 - 10: Build the final kriging model based on the adjusted SEC signal.
 - 11: Run the final kriging model to develop improved additive strain maps.
-

2.2. Kriging (gaussian process regression)

Kriging (or Gaussian process regression) is a statistical process in which interpolated values are obtained from a spatially dependent set of training data. As a general rule, kriging seeks to predict the value of a function at the point of interest by computing a spatially weighted average of the training points in the neighborhood [42, 47]. The spatial variability of a generalized spatially continuous process at a location x , denoted as $\mathbf{Z}(x)$, can be represented as:

$$\mathbf{Z}(x) = \mu(x) + \epsilon(x), \quad (4)$$

where $\mu(x)$ is the mean value of the process and $\epsilon(x)$ deals with the small-scale spatial variation in the process. When considering a noisy process, $\epsilon(x)$ is typically related to the noise (i.e. error) term. In cases where the prediction mean $\mu(x)$ varies smoothly, universal kriging (sometimes called kriging with external drifts or regression kriging) is preferred [48]. When considering external drifts and expressing n observations (training points) as $z(x_1), z(x_2), \dots, z(x_n)$, the value at a new, unsampled location x_0 can be predicted as the sum of the drift component (\hat{m}) plus the residual ($\hat{\epsilon}$):

$$\hat{z}(x_0) = \hat{m}(x_0) + \hat{\epsilon}(x_0), \quad (5)$$

where the drift term \hat{m} is fit onto an assumed trend term using linear regression. Various trend terms have been used to model the large-scale spatial variations in the sample data and these terms include linear, polynomial, and point logarithmic [49]. This work uses a regional linear trend to estimate the mean value at x_0 [50]. The universal kriging predicted value $\hat{z}(x_0)$ can be solved for in a matrix notation as:

$$\hat{z}(x_0) = \mathbf{q}_0^T \cdot \hat{\beta} + \lambda_0^T \cdot \mathbf{e}, \quad (6)$$

where \mathbf{q}_0 is a vector of the predictors at x_0 , $\hat{\beta}$ is a vector that contains the estimated drift term coefficients, λ_0 is a vector of n kriging weights determined by the covariance function, and

\mathbf{e} is a vector that contains all the regression residuals. The unknown drift term coefficients, $\hat{\beta}$, can be solved for using the generalized least squares technique, formulated as:

$$\hat{\beta} = (\mathbf{q}^T \cdot \mathbf{C}^{-1} \cdot \mathbf{q})^{-1} \cdot \mathbf{q}^T \cdot \mathbf{C}^{-1} \cdot \mathbf{z}, \quad (7)$$

where \mathbf{q} is the matrix of the predictors at all observed locations, \mathbf{z} is the sampled observations, and \mathbf{C} is the covariance matrix of residuals:

$$\mathbf{C} = \begin{bmatrix} C(x_1, x_2) & \cdots & C(x_1, x_n) \\ \vdots & \ddots & \vdots \\ C(x_n, x_1) & \cdots & C(x_n, x_n) \end{bmatrix}. \quad (8)$$

The covariance between point pairs $C(x_i, x_j)$, separated by a distance d , in the covariance matrix are then estimated using a variogram model. Different forms of variogram models (variance functions) have been developed to model the spatial correlation in the random space between point pairs. Examples of variogram models include the Gaussian, exponential, spherical, linear and power models. For the purpose of this work, the power model was selected due to its simplicity and capability to estimate unbounded spatial variances [51]. The power variogram model is expressed as $s \cdot d^\alpha + n$, and used to form the piecewise semivariance function $\gamma(d)$:

$$\gamma(d) = \begin{cases} 0 & d = 0 \\ s \cdot d^\alpha + n & 0 \leq d \end{cases} \quad (9)$$

where s is a scaling factor, α is the exponent (between 1 and 1.99), and n is the nugget term [50]. The nugget term accounts for the 'noise' in the measurement as it represents the random deviations from the otherwise smooth spatial data trend. $\gamma(d)$ is related with the covariance function for a point wise pair as $\gamma(d) = n - C(x_i, x_j)$. As represented in equation (9), this work considers measurements that are 'exact', meaning that at the training points the variogram is forced to be zero (i.e. the predicted values at the training points will be equal to the observed values at these points). Lastly, considering that the generalized least squares accounts for the spatial correlation of residuals, equation (6) can be expressed as:

$$\hat{z}(x_0) = \mathbf{q}_0^T \cdot \hat{\beta} + \lambda_0^T \cdot (\mathbf{z} - \mathbf{q} \cdot \hat{\beta}). \quad (10)$$

Given that various points of interest are sampled with sufficient density, the universal kriging process outlined here can create a near continuous interpolation of a sampled process. More details about the kriging model can be found in [50]. This work utilized PyKriging, an open source kriging toolkit for Python, for the development and solving of the universal kriging interpolation models [52].

3. Strain map adjustment algorithm

The use of traditional interpolation methods (including kriging and radial basis functions) for the estimation of full-field strain maps for structures monitored by an SEC-based sensing skin only considers the sensor location and signal. For these interpolation methods, the signal of each SEC is deemed to be located at the center of the sensor. The proposed strain map

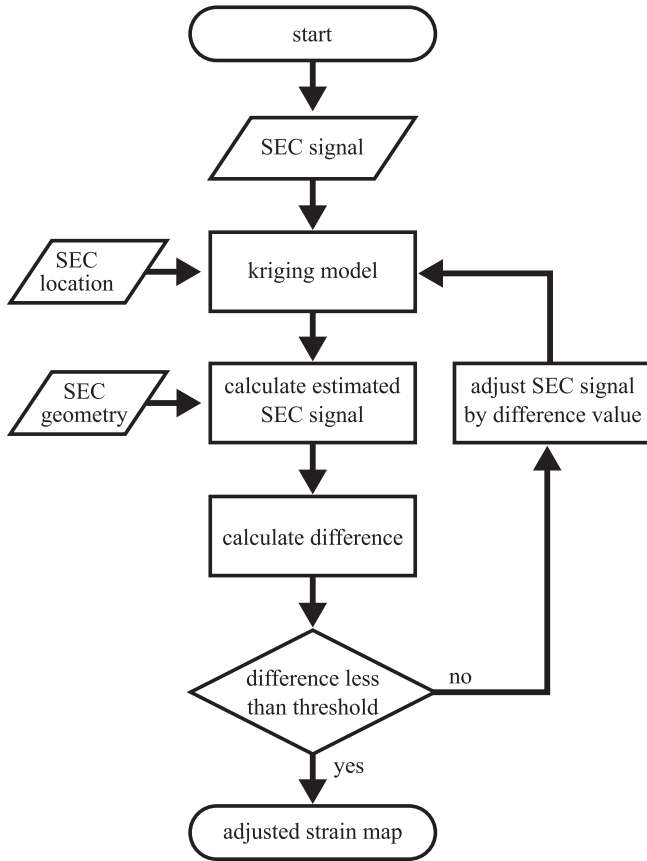


Figure 2. Flowchart detailing the strain map adjustment algorithm.

adjustment algorithm improves the accuracy of the full-field strain maps by fusing the sensor geometry, along with the sensor location and signal, into the strain maps.

The proposed algorithm maintains the assumption that the signal of the SEC is located at the center of the SEC. However, the additive strain measured by the sensor corresponds to the average strain under the sensing area, and is therefore not equal to the additive strain found at the center. It should also be noted that the discrepancy between these two values increases with either an increase in sensor size or an increase in strain map complexity. The proposed strain map adjustment algorithm is presented as a flowchart in figure 2, described as a pseudocode in algorithm 1, and discussed it what follows. First, a universal kriging model, denoted as UK in the following equations, is trained using the SEC sensor locations \mathbf{I}^{SEC} and their measured additive strain data \mathbf{O}^{SEC} :

$$\varepsilon(x, y) = \text{UK}((x, y) | \mathcal{D} = \{\{\mathbf{I}^{\text{SEC}}, \mathbf{O}^{\text{SEC}}\}\}), \quad (11)$$

where $\varepsilon(x, y)$ is the additive strain at an arbitrary point (x, y) . The Gaussian process or kriging model for this arbitrary point is denoted $\text{UK}((x, y) | \mathcal{D})$ where \mathcal{D} is the data set used for training the model. Considering an SEC sensor location i , the average strain value for the area monitored by the sensor, written as $O_i^{\text{SEC,estimated}}$, is extracted from the 2D additive

strain field $\varepsilon(x, y)$ such that:

$$O_i^{\text{SEC,estimated}} = \frac{1}{n} \sum_{z=1}^n \varepsilon(x_z, y_z), \quad (12)$$

where n is the number of strain points under the SEC sensor i that are sampled from the kriging model. Next, the difference between the measured strain for a sensor (O_i^{SEC}) and the strain estimated by the kriging model at that location ($O_i^{\text{SEC,estimated}}$) is given by:

$$\xi_i = O_i^{\text{SEC}} - O_i^{\text{SEC,estimated}}. \quad (13)$$

Once ξ_i has been solved for, it is used to update the strain value measured by the sensor (O_i^{SEC}) and create an adjusted SEC signal value:

$$O_i^{\text{SEC,adjusted}} = O_i^{\text{SEC}} + \xi_i. \quad (14)$$

Combining $O_i^{\text{SEC,adjusted}}$ for all sensors in the sensing skin yields the vector $\mathbf{O}^{\text{SEC,adjusted}}$. These adjusted strain values, resulting from a fusion of SEC signals, locations, and geometries, are used to train a new kriging model:

$$\varepsilon(x, y) = \text{UK}((x, y) | \mathcal{D} = \{\{\mathbf{I}^{\text{SEC}}, \mathbf{O}^{\text{SEC,adjusted}}\}\}) \quad (15)$$

and therefore, a new additive strain field $\varepsilon(x, y)$. This process of obtaining estimated SEC strain signals from the kriging-estimated strain field, adjusting the SEC signals based on the difference between the real and estimated signals, and resolving the kriging-estimated strain field based on the adjusted signals is repeated until a stop condition is met. In this work, the stop condition requires every ξ_i to fall below $0.1 \mu\varepsilon$.

A graphical representation of the strain map adjustment algorithm for a simplified 1D case is presented in figure 3. This 1D pseudo strain data was created to represent a relatively complex strain topography that is monitored by five SECs. The measurement of each SEC is the mean strain over the area monitored by the SEC. The real strain distribution is represented by the thin black line with the real strain value at the center of the SEC denoted by the filled black circles. The geometric transition from one SEC to another is denoted by the dotted vertical line. The strain map adjustment algorithm starts with the strain value measured by the i th SEC from the real strain distribution to form the data point O_i^{SEC} . For the purpose of this simplified 1D case, this measurement is obtained without considering any noise in the signal and is represented by the hollow black circle in figure 3. These strain measurements can be observed to correctly estimate the strain value at the center of the sensor for sensor locations that monitor linear strain distributions (i.e. SECs 1, 4, and 5) while either overestimating or underestimating the strain value for locations that monitor more complex strain distributions (i.e. SECs 2 and 4). Once the SEC measurements have been obtained, a kriging model is generated that uses the SEC-measured strain as the input for the model, this model is then densely sampled over the entire distance to create a near continuous strain distribution as represented by the dashed blue line. Note that the model goes through the data points used in training the model and as such this initially estimated strain distribution can be observed to overestimate the strain

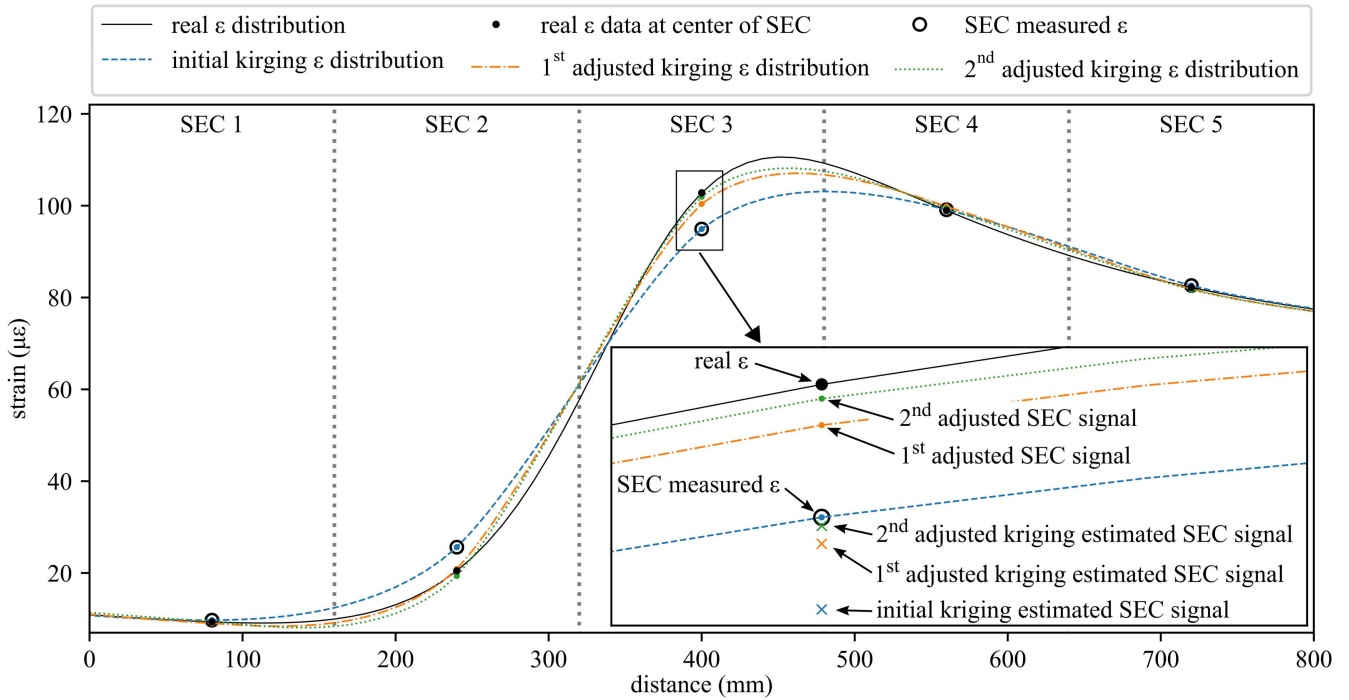


Figure 3. Graphical representation of the first three iterations of the strain map adjustment algorithm for a 1D pseudo strain data monitored by 5 SECs with the inset showing a closeup of SEC 3.

at SEC 2 and underestimate the strain at SEC 3. Now the estimated SEC signal ($O_i^{\text{SEC,estimated}}$) is obtained from the densely sampled initial kriging model, and for $i = 3$ (SEC 3), this value is shown as a blue x in the inset of figure 3. Next the difference between O_i^{SEC} and $O_i^{\text{SEC,estimated}}$ can be calculated from equation (13) and used to adjust the SEC signal used in training the adjusted kriging model (or the next adjusted SEC signal in the case of additional iterations) as denoted in equation (14). This newly adjusted SEC signal is represented by an orange filled circle in the inset of figure 3 and is termed the 1st adjusted SEC signal. This process is repeated until the adjusted SEC signal converges to the measured SEC signal. These adjusted SEC signals, which are closer to the real strain values at the center of the SEC, can then be used to generate kriging models that better reproduce the shape of the strain topology over the entire area of interest. For this example, only two iterations are required to generate a kriging model that shows a marked improvement over the original kriging-estimated strain topography as shown by the dotted green line in figure 3.

4. Methodology

This section starts by introducing the experimental test setup that forms the basis for both the numerical validation and experimental verification performed in this work. After, a brief noise quantification study is performed on an SEC from the experimental setup to provide realistic noise characteristics for the numerical study. Lastly, the numerical and experimental studies are presented.

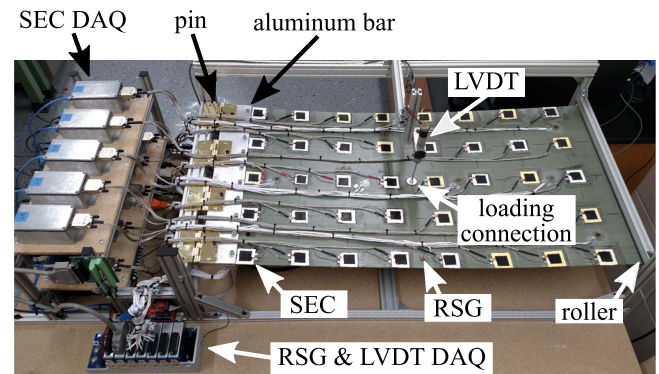


Figure 4. Experimental setup used as the basis for the numerical validation and for generating experimental data used in this work.

4.1. Experimental setup

The strain map adjustment algorithm presented in this work is numerically validated and experimentally verified using the configuration shown in figure 4. The numerical investigation is conducted on an FEA model of the plate for a variety of sensor layouts. The experimental test setup consists of a fiberglass plate with a geometry of $500 \times 900 \times 2.6 \text{ mm}^3$. The plate is driven by a stepper motor mounted under the plate and connected to the plate through a series of mechanical linkages. The left-hand side of the plate is bolted to an aluminum support ($12.7 \times 76.2 \times 500 \text{ mm}^3$). This bolted connection forms a rigid connection that was added to eliminate strain complexities from a direct connection of the hinge to the fiberglass plate. This rigid connection is attached to the frame through a pinned connection. The right-hand side of the plate is restrained in the vertical direction by a roller.

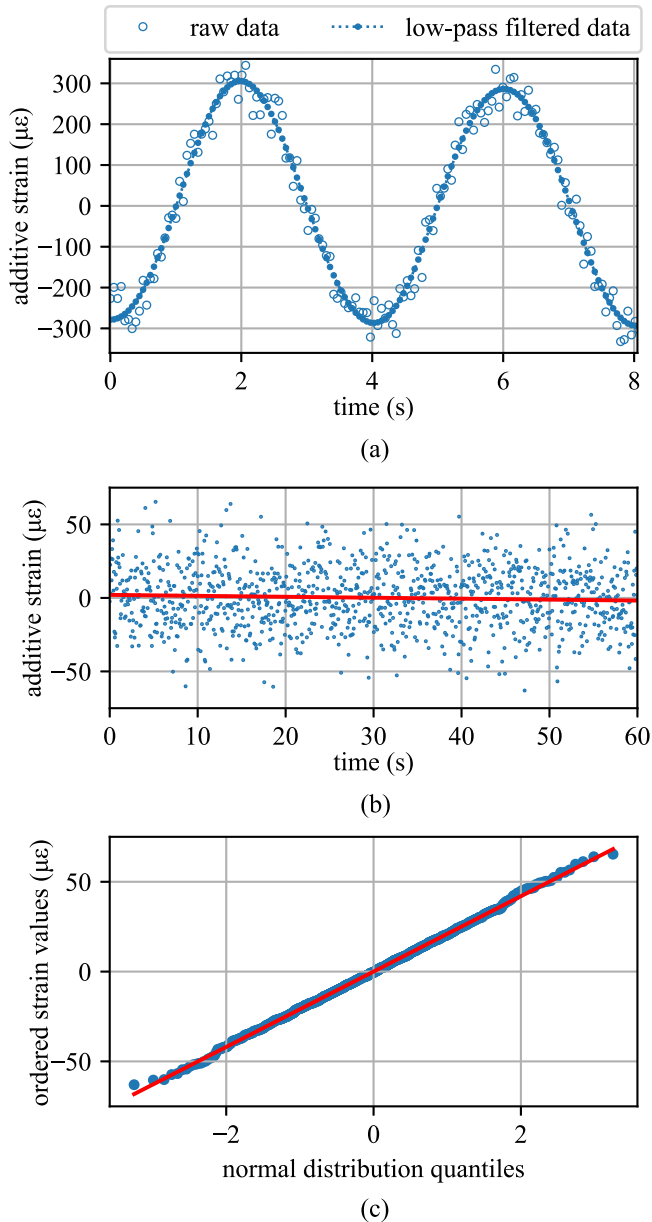


Figure 5. Experimental data for a sensor on the experimental test setup used showing: (a) dynamic response for a sinusoidal input load; (b) static response for a constant load; and (c) q–q plot of the static load compared to a normal distribution.

This roller consists of two lightly greased rods of diameter 12.7 mm mounted on both the top and bottom of the plate. This experimental setup was previously used in a study related to developing uni-directional strain maps from the SEC-based sensing skin [35].

4.2. SEC noise quantification

A noise signature is extracted from the experimental test setup for the SEC sensor just to the left of the loading point in figure 4 for the purpose of evaluating the robustness of the strain map adjustment algorithm with respect to noise. The SEC was selected at this location as it experienced a relatively

Table 1. Parameters used in constructing the FEA model.

Parameter	Value
Elements total	298 065
Elements type	linear brick
Abaqus element type	C3D8R
Elements (aluminum connection)	32 340
Elements (fiberglass plate)	265 725
Element nodes	8
Element integration points	1
Young's Modulus (aluminum)	68.9 GPa
Young's Modulus (fiberglass)	15 GPa
Poisson's ratio (aluminum)	0.33
Poisson's ratio (fiberglass)	0.21
Density (aluminum)	2700 kg m ⁻³
Density (fiberglass)	2100 kg m ⁻³
Plate dimensions	500 × 900 × 3.18 mm ³

high level of strain during dynamic testing and the length of the cable connecting the SEC sensor to the DAQ is of average length. Figure 5 presents the data for the single sensor under a dynamic (figure 5(a)) and static (figure 5(b)) load case. The experimental data for the static load case, sampled at 17 samples per second, was found to have a standard deviation of $\sigma = 32 \mu\epsilon$. The red line in figure 5(b) is the best-fit linear regression of the data over the 60 s test. In total, the data was found to drift $4.12 \mu\epsilon$ with r - and p -values of -0.056 and 0.048 respectively. The capability of a normal distribution to effectively estimate the SEC signal noise is demonstrated by the q–q plot presented in figure 5(c). Therefore, a noise with a normal distribution and a standard deviation of $\sigma = 32 \mu\epsilon$ is deemed appropriate for conducting simulations of the strain map adjustment algorithm with respect to noise.

4.3. Numerical validation

Numerical validation of the strain map adjustment algorithm is performed using 10 load cases of varying complexities applied to an Abaqus FEA model of the experimental test setup [53]. The FEA model was designed to replicate the experimental test setup. In addition to modeling the fiberglass plate, the FEA model also considers the rigid aluminum connection on the left-hand side of the plate. The model is constructed of 298 065 linear brick elements, each with eight-nodes and one integration point. This model configuration was found to have an error of less than 1% when compared to a densely meshed (1.2 million elements) version of the same FEA model. In the fiberglass plate, nine elements are used through its thickness to prevent shear locking. The plate's connection, pinned on the left-hand side and a roller on the right-hand side, were modeled as ideal connections. The material properties of the fiberglass were obtained experimentally while the properties of the aluminum were taken from the material's data sheet supplied by the distributor. The key parameters of the FEA model are listed in table 1.

The 10 loading cases are presented using figure 6 and table 2 where figure 6 details the locations of the seven loading location identifiers (A–F) consisting of four loading

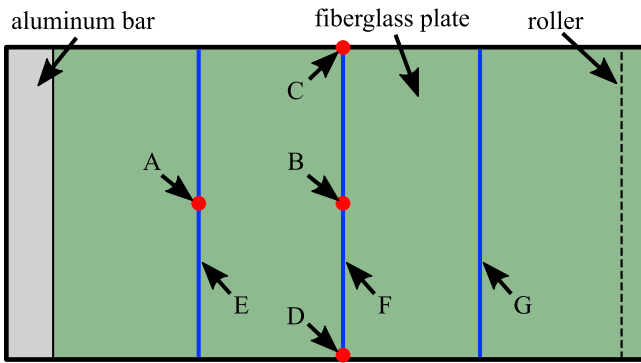


Figure 6. Schematic representation of the experimental plate with the identifiers (A–F) used for annotating the loading points for the ten load cases presented in table 2.

Table 2. Displacements associated with the identifiers (A–F) from figure 6 for the 10 loading conditions considered for this study.

	Displacement (mm)						
	A	B	C	D	E	F	G
Load case 1		5					
Load case 2	5						
Load case 3	0	5					
Load case 4			5				
Load case 5				5	0		
Load case 6					5		
Load case 7						5	
Load case 8							5
Load case 9					5		5
Load case 10					5	0	5

points (A–D) and three uniform loading conditions (E–G). Table 2 lists the displacement for each of the identifiers for the 10 load cases considered. In the case that a specific location is unused for a load case, its correlating position in table 2 is left empty. A displacement of zero denotes a loading point that is fixed at 0 mm of displacement. The strain maps produced for these 10 load cases are shown in figure 7. These load cases were selected to develop strain maps that produced varying amounts of asymmetry and strain map complexity. For each load case, the strain maps are normalized to either their maximum compressive or tensile strain values to help the visualization of results such that the no strain condition is the same color for each plot. The values associated with the maximum compressive and tensile strain for the load cases are listed in table 3.

The numerical validation also investigated the effect of changing sensor densities on the accuracy of both the traditional kriging and adjusted kriging strain maps. To do this, an algorithm was formulated that covered the monitored area of the fiberglass plate with an evenly spaced grid of square SEC sensors. This algorithm started with six sensors and progressively added square sensors to the fiberglass plate by reducing the size of each individual sensor. Every combination of square sensors arranged in a rectangular grid formed from six to 500 sensors was considered, with a total of 39

different grid configurations considered. Figure 8 shows the SEC sensor layouts for three different sensor densities. As the strain map adjustment algorithm seeks to only update the strain value at the center of each SEC, the spaces between the SECs do not have a direct effect on the strain map interpolations. However, this unmonitored area does have a secondary effect on the performance of the algorithm as an area that is not monitored by a sensor will not be fused into the adjusted additive strain map. For uniformity, this work considers only SEC sensors of a square geometry. The investigation of other dense sensor network configurations, including those with non-uniform sensor densities, geometries, and sizes, are beyond the scope of this introductory work.

4.4. Experimental verification

The experimental verification for the strain map adjustment algorithm was performed using a network of 40 SECs deployed as a grid onto the fiberglass plate. The layout of these SECs is presented in figure 9. In addition to the 40 SECs, 20 RSGs were deployed onto the fiberglass plate for the purpose of validating the strain map adjustment algorithm at various locations on the plate. The RSGs (model #FCA-5-350-11-3LJBT, manufactured by Tokyo Sokki Kenkyujo) were deployed in pairs, each individually measuring ϵ_x and ϵ_y . The 40 SECs were deployed in a 5×8 grid array, each monitoring an area of $38 \times 38 \text{ mm}^2$. The DAQ system consists of 10 custom-built capacitance measurement devices (annotated as SEC DAQ in figure 4) that also generate an active shield for the cable that removes the parasitic capacitance found in the cable. In addition to these devices, a chassis (cDAQ-9178, manufactured by National Instruments) was used to hold three quarter bridge analog input (NI-9236) modules for measuring the RSGs, an analog input module (NI-9205) for measuring the LVDT, and a digital output module (NI-9472) for sourcing a trigger to ensure the SEC and RSG data is sampled simultaneously. Additionally, an LVDT (model #0244, manufactured by Trans-Tek) was mounted to the plate to record the plates center displacement. All the data sources were measured at 17 samples per second. Lastly, to remove the high-frequency noise found in the SEC signal, a fifth-order Butterworth filter with a cutoff frequency of 10 Hz was used. The effects of this filtering can be seen in figure 5(a). No filtering was needed for either the RSG or LVDT data.

The experimental validation considered two experimental load cases. First, load case 1 (similar to load case 1 in the numerical investigation) is used to verify the strain map adjustment algorithm for a relatively simple load case. This load case is produced at the center of the plate by the stepper motor located under the plate. The plate is displaced 5 mm from its initial condition harmonically at 0.25 Hz. Second, an asymmetric load is generated to verify the strain map adjustment algorithm under a more complex loading condition. To generate this asymmetric load, a 0.5 kg mass is added at the center of the plate along its top edge (see figure 9) then the plate is excited using the stepper motor in the same

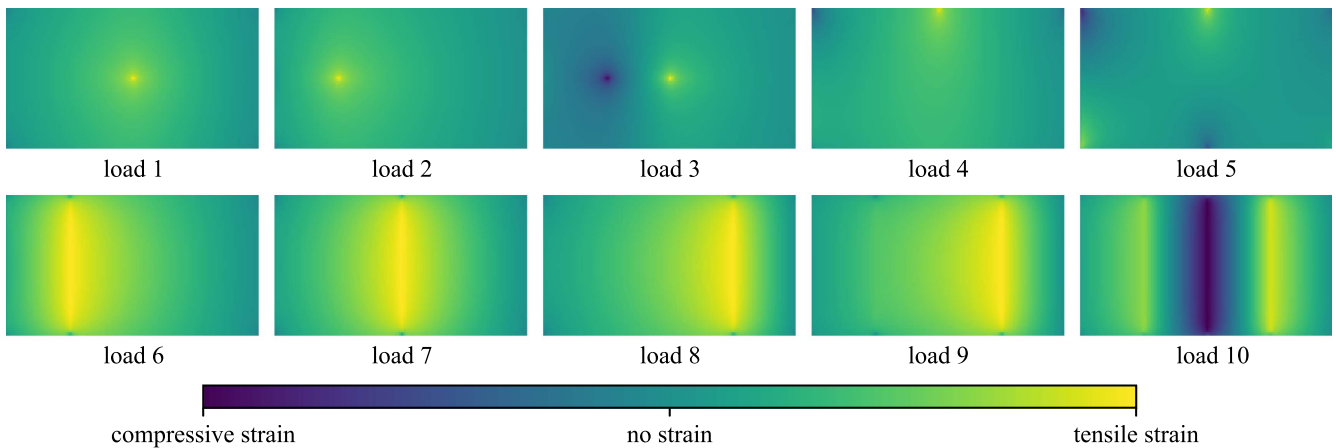


Figure 7. Additive strain maps, generated by the FEA model, for the ten load cases used in the numerical analysis portion of this work. Numerical values for the maximum compressive and tensile strains are listed in table 3.

Table 3. Values associated with the maximum compressive and tensile strain for the load cases presented in figure 7.

	Maximum compressive strain ($\mu\epsilon$)	Maximum tensile strain ($\mu\epsilon$)
Load case 1	-1572	1572
Load case 2	-1938	1938
Load case 3	-7160	7160
Load case 4	-1135	1135
Load case 5	-1965	1965
Load case 6	-1043	1043
Load case 7	-907	907
Load case 8	-1266	1266
Load case 9	-1239	1239
Load case 10	-6797	6797

manner as load case 1. For both cases, the experimental data is investigated over two complete cycles.

5. Results

This section presents the results from both the numerical and experimental studies. First, a detailed evaluation of the strain map adjustment algorithm for load case 4 is presented, followed by a discussion on the results for all ten load cases. Lastly, the experimental results are discussed.

5.1. Numerical validation

Results for the strain map adjustment algorithm for load case 4, monitored with 28 SECs as shown in figure 8(b), are presented in figure 10. The combination of load case 4 with 28 SECs was selected due to its capability to demonstrate both portions of the strain field where the strain map adjustment algorithm improves the accuracy of the strain map (i.e. near the load case) and portions where its benefit is less obvious (i.e. portions the strain topography that are relatively simple). To expand, figure 10 presents both the plate's real strain map and its kriging-estimated strain maps using the

traditional kriging method (figure 10(a)) and the strain map adjustment algorithm (figure 10(b)). Figure 10(c) reports the RMSE error between the real strain map and that estimated using the strain map adjustment algorithm over each successive iteration of the algorithm. In figure 10(c) the initial condition is the strain map generated using a traditional kriging method (figure 10(a)) and therefore does not incorporate the sensor geometry into the strain map interpolation. Conversely, the strain map for iteration 16 (figure 10(b)) incorporates the sensor geometry into the reconstructed strain maps. The inset in figure 10(c) shows the reduction in strain map reconstruction error (measured as $\mu\epsilon$) by the strain map adjustment algorithm (figure 10(b)) over the traditional kriging method (figure 10(a)). The strain map adjustment algorithm generates a considerable improvement near the loading point at the top center of the plate where the traditional kriging method underestimates the real strain value. Furthermore, the algorithm generally improves the accuracy of the strain map over the entire plate.

Figure 11 reports the results for the ten cases used in the numerical validation in terms of the root mean squared error (RMSE) where the error is measured at every point of the strain map. Results are reported for the RMSE from both the traditional kriging method and for the strain map adjustment algorithm. These results are reported with and without noise added to the system. Overall, the strain maps developed using the strain map adjustment algorithm have less error than those developed using the traditional method. A few notable results for some specific load cases are as follows. First, it should be noted that in every load case considered for the no-noise conditions the adjusted strain maps are capable of achieving a level of error that would require far more sensors than if the strain map adjustment algorithm was not used. When noise was added to the sensor signal and for loading conditions that developed low levels of strain (e.g. load cases 1, 4, and 7), the benefit of using the strain map adjustment algorithm for a given number of SECs was reduced but never worse than the traditional kriging method's error levels. Next, it can be noticed that load cases 4 and 5 experience an increase in error for an increase in the number of sensors deployed in the dense

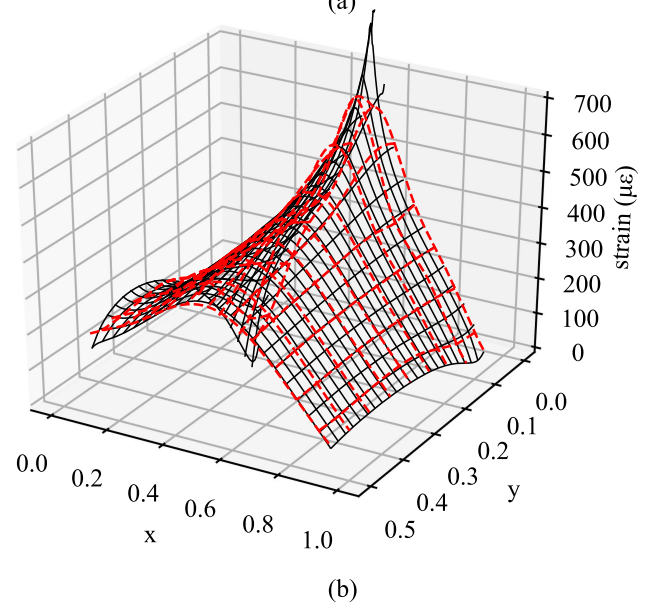
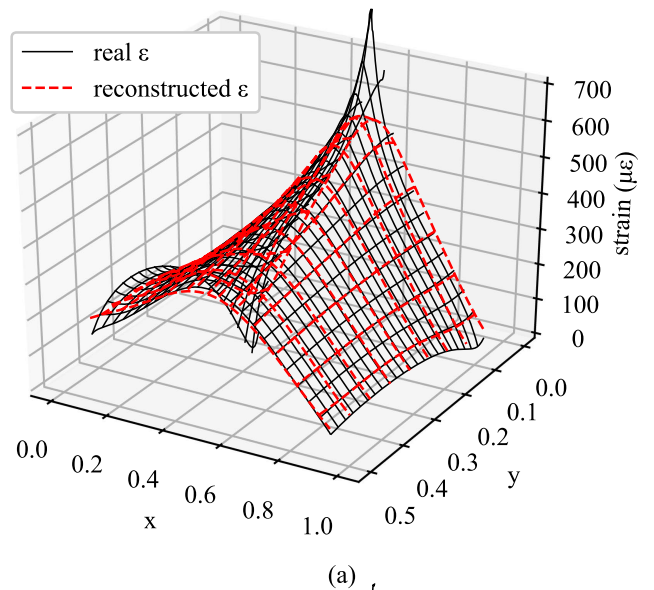
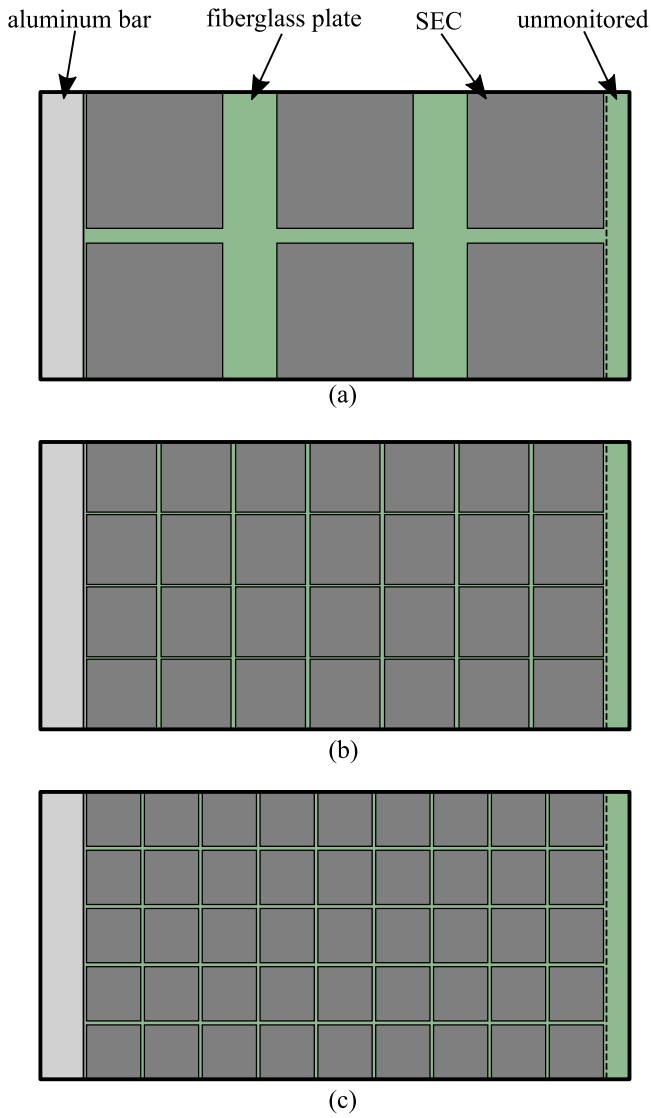


Figure 8. SEC-based sensing skin layouts with: (a) six SECs; (b) 28 SECs; and (c) 45 SECs.

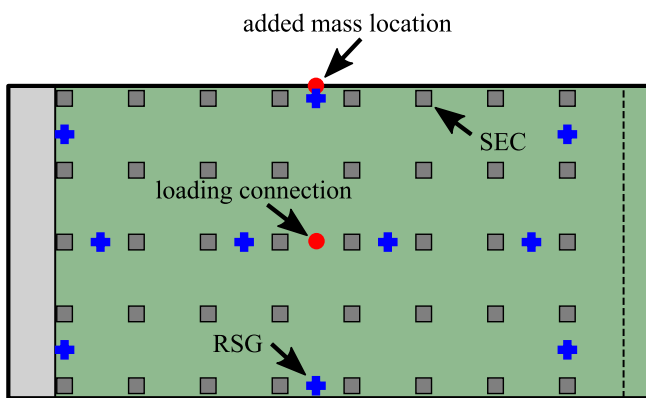


Figure 9. SEC and RSG layout of the experimental test setup used for experimental validation.

sensor network before leveling out once a certain number of sensors are used. This increase in RMSE for load cases 4 and 5 come from the very center of the plate where the kriging method underestimates the peak strain value due to sensors

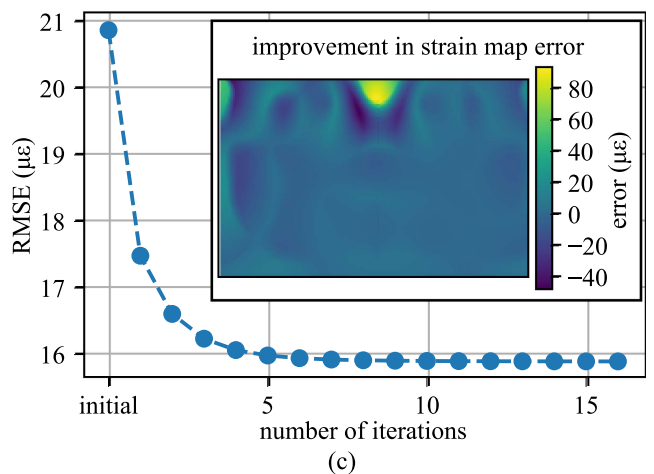


Figure 10. Strain maps generated for load case 4: (a) using the traditional kriging method; (b) using the strain map adjustment algorithm; and (c) showing the RMSE as a function of number of iterations for the strain map adjustment algorithm where the inset shows the improvement in strain between the traditional kriging method and the proposed algorithm.

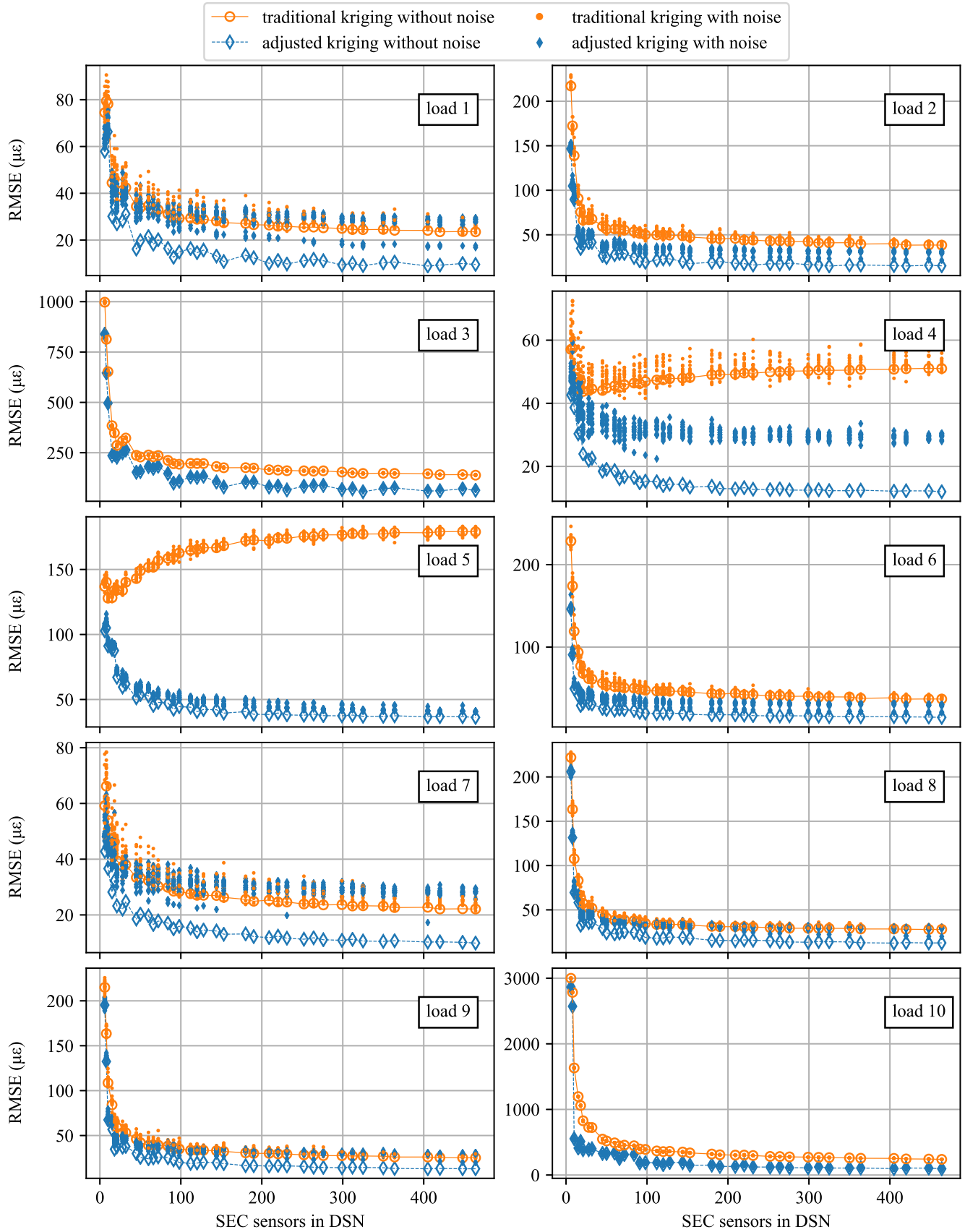


Figure 11. RMSE results for both the traditional kriging and the adjusted kriging methods for all ten load cases, considered both with and without noise.

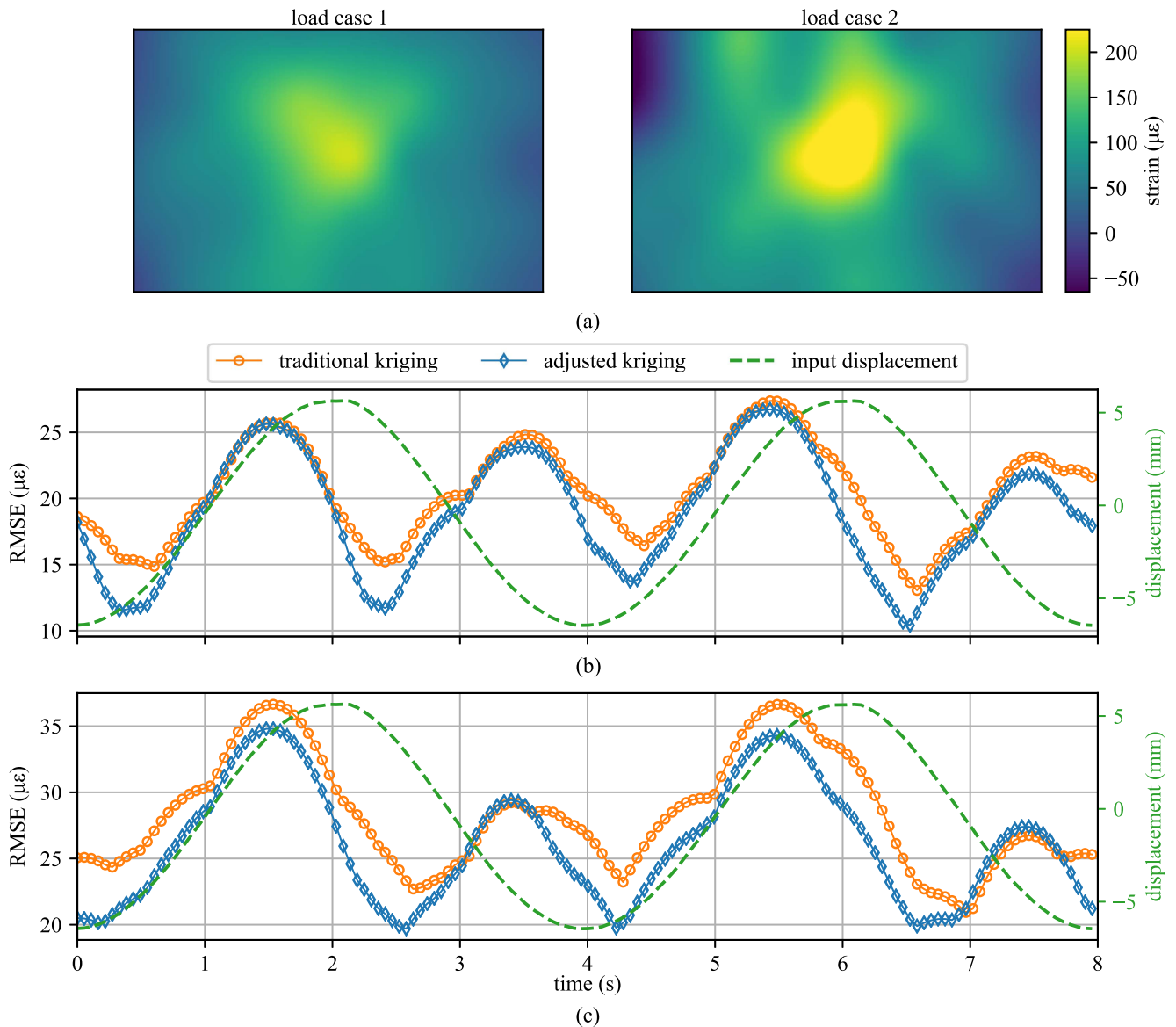


Figure 12. Temporal RMSE results for the 0.25 Hz loading condition under the experimental: (a) load case 1; and (b) load case 2. A video form of this figure is available as a supplementary material for this article at [stacks.iop.org/sms/27/075033/mmedia]

being positioned right on top of this high strain concentration. However, in both of these cases, the strain map adjustment algorithm is capable of compensating for this concentrated strain location.

5.2. Experimental verification

The experimental results for the 40 sensors deployed on the experimental test setup are presented in figure 12. The strain maps in figure 12(a) report the full-field strain maps developed using the strain map adjustment algorithms for both load cases. For the experimental study the RMSE is measured at the 20 RSG locations on the plate. The RSGs are used for this task due to their higher accuracy when compared to the SECs, and capability to measure the additive strain at any location when their signals are added together. As expected, the RMSE for both load cases generally increases when the displacement is increasing and is near either its maximum

upward or maximum downward displacement. Load case 1 (figure 12(b)) does report lower error values than load case 2 (figure 12(c)). This increase in the error for load case 2 is to be expected given the general increase in the complexity of the strain topography for load case 2, as seen in figure 12(a). Additionally, for two brief moments in load case 2 around 3.4 and 7.4 s, the adjusted strain map reports a higher level of error than those generated using the traditional kriging methods. This can be attributed to the relatively small number of RSG gauges used for quantifying the error of the full-field strain maps.

6. Conclusion

This work proposed an algorithm that fuses the locations of strain sensors, their signals, and the geometry of a network of



sensors constituting a sensing skin into an approximated full-field strain map. These sensors, termed SECs, are a large-area electronic that are capable of covering large areas at low costs. Given that each SEC measures the summation of a structure's orthogonal strains (i.e. $\varepsilon_x + \varepsilon_y$), the SECs deployed in a network configuration are capable of reproducing the full-field additive strain map of a structure. These full-field strain maps can then be used to extract physics-based features for real-time condition assessment. Examples of the physics-based features include changes in strain maps and deflection shapes.

The proposed algorithm improves the quality of these full-field strain maps by fusing the sensor size into a traditional strain field interpolation that only uses the sensor location and signal. This work used kriging as the interpolation method. However, other interpolation methods including cubic splines and radial bias functions could also be used. The improvement in the additive full-field strain map generation is accomplished through iterative adjustments to the measured SEC signal used as the input to the kriging model until the measured SEC signal matches the SEC signal estimated using the kriging model. Therefore, the newly proposed algorithm fuses data from the SEC's location, signal, and geometry to produce a full-field strain map. Results from numerical and experimental investigations show that the proposed strain map adjustment algorithm is capable of generating improved full-field strain maps over those produced using the traditional kriging method.

Acknowledgments

This work was in part supported by the National Science Foundation Grant Nos. CNS-1566579 and ECCS-1611333. This work was also partly supported by the National Science Foundation Grant No. 1069283, which supports the activities of the Integrative Graduate Education and Research Traineeship (IGERT) in Wind Energy Science, Engineering and Policy (WESEP) at Iowa State University. Their support is gratefully acknowledged. Any opinions, findings, and conclusions or recommendations expressed in this material are those of the authors and do not necessarily reflect the views of the National Science Foundation.

ORCID iDs

Austin Downey  <https://orcid.org/0000-0002-5524-2416>
 Mohammadkazem Sadoughi  <https://orcid.org/0000-0002-6106-3318>
 Simon Laflamme  <https://orcid.org/0000-0002-0601-9664>
 Chao Hu  <https://orcid.org/0000-0001-9228-7675>

References

- [1] Lynch J P, Farrar C R and Michaels J E 2016 Structural health monitoring: technological advances to practical implementations [scanning the issue] *Proc. IEEE* **104** 1508–12
- [2] Yao Y, Tung S-T E and Glisic B 2014 Crack detection and characterization techniques-an overview *Struct. Control Health Monit.* **21** 1387–413
- [3] Posenato D, Lanata F, Inaudi D and Smith I F C 2008 Model-free data interpretation for continuous monitoring of complex structures *Adv. Eng. Inform.* **22** 135–44
- [4] Enckell M, Glisic B, Myrvoll F and Bergstrand B 2011 Evaluation of a large-scale bridge strain, temperature and crack monitoring with distributed fibre optic sensors *J. Civil Struct. Health Monit.* **1** 37–46
- [5] Lynch J P, Sundararajan A, Law K H, Kiremidjian A S and Carryer E 2004 Embedding damage detection algorithms in a wireless sensing unit for operational power efficiency *Smart Mater. Struct.* **13** 800–10
- [6] Perry M, McAlorum J, Fusiek G, Niewczas P, McKeeman I and Rubert T 2017 Crack monitoring of operational wind turbine foundations *Sensors* **17** 1925
- [7] Tikka J, Hedman R and Siljander A 2003 Strain gauge capabilities in crack detection *4th Int. Workshop on Structural Health Monitoring* pp 15–7
- [8] Tung S-T, Yao Y and Glisic B 2014 Sensing sheet: the sensitivity of thin-film full-bridge strain sensors for crack detection and characterization *Meas. Sci. Technol.* **25** 075602
- [9] Lee H M, Kim J M, Sho K and Park H S 2010 A wireless vibrating wire sensor node for continuous structural health monitoring *Smart Mater. Struct.* **19** 055004
- [10] Wang Y, Gong J, Dong B, Wang D Y, Shillig T J and Wang A 2012 A large serial time-division multiplexed fiber bragg grating sensor network *J. Lightwave Technol.* **30** 2751–6
- [11] Loh K J, Hou T-C, Lynch J P and Kotov N A 2009 Carbon nanotube sensing skins for spatial strain and impact damage identification *J. Nondestruct. Eval.* **28** 9–25
- [12] Hua P, Woo E J, Webster J G and Tompkins W J 1993 Finite element modeling of electrode-skin contact impedance in electrical impedance tomography *IEEE Trans. Biomed. Eng.* **40** 335–43
- [13] Hallaji M, Seppänen A and Pour-Ghaz M 2014 Electrical impedance tomography-based sensing skin for quantitative imaging of damage in concrete *Smart Mater. Struct.* **23** 085001
- [14] Zhang Y 2006 In situ fatigue crack detection using piezoelectric paint sensor *J. Intell. Mater. Syst. Struct.* **17** 843–52
- [15] Hou T-C and Lynch J P 2008 Electrical impedance tomographic methods for sensing strain fields and crack damage in cementitious structures *J. Intell. Mater. Syst. Struct.* **20** 1363–79
- [16] Borcea L 2002 Electrical impedance tomography *Inverse Problems* **18** R99–136
- [17] Downey A, D'Alessandro A, Baquera M, García-Macías E, Rolfes D, Ubertini F, Laflamme S and Castro-Triguero R 2017 Damage detection, localization and quantification in conductive smart concrete structures using a resistor mesh model *Eng. Struct.* **148** 935
- [18] Downey A, D'Alessandro A, Ubertini F and Laflamme S 2017 Automated crack detection in conductive smart-concrete structures using a resistor mesh model *Meas. Sci. Technol.* **29** 035107
- [19] Pan B, Qian K, Xie H and Asundi A 2009 Two-dimensional digital image correlation for in-plane displacement and strain measurement: a review *Meas. Sci. Technol.* **20** 062001
- [20] Ryu D and Loh K J 2012 Strain sensing using photocurrent generated by photoactive p3ht-based nanocomposites *Smart Mater. Struct.* **21** 065016
- [21] Arias A C, MacKenzie J D, McCulloch I, Rivnay J and Salleo A 2010 Materials and applications for large area electronics: Solution-based approaches *Chem. Rev.* **110** 3–24

- [22] Paradiso J A, Lifton J and Broxton M 2004 Sensate media—multimodal electronic skins as dense sensor networks *BT Technol. J.* **22** 32–44
- [23] Glisic B, Yao Y, Tung S-T E, Wagner S, Sturm J C and Verma N 2016 Strain sensing sheets for structural health monitoring based on large-area electronics and integrated circuits *Proc. IEEE* **104** 1513–28
- [24] Hu Y, Rieutort-Louis W S A, Sanz-Robinson J, Huang L, Glisic B, Sturm J C, Wagner S and Verma N 2014 Large-scale sensing system combining large-area electronics and CMOS ICs for structural-health monitoring *IEEE J. Solid-State Circuits* **49** 513–23
- [25] Kang I, Schulz M J, Kim J H, Shanov V and Shi D 2006 A carbon nanotube strain sensor for structural health monitoring *Smart Mater. Struct.* **15** 737–48
- [26] Loh K J, Kim J, Lynch J P, Kam N W S and Kotov N A 2007 Multifunctional layer-by-layer carbon nanotube–polyelectrolyte thin films for strain and corrosion sensing *Smart Mater. Struct.* **16** 429–38
- [27] Robert C, Feller J F and Castro M 2012 Sensing skin for strain monitoring made of PC-CNT conductive polymer nanocomposite sprayed layer by layer *ACS Appl. Mater. Interfaces* **4** 3508–16
- [28] Burton A R, Lynch J P, Kurata M and Law K H 2017 Fully integrated carbon nanotube composite thin film strain sensors on flexible substrates for structural health monitoring *Smart Mater. Struct.* **26** 095052
- [29] Luo S, Hoang P T and Liu T 2016 Direct laser writing for creating porous graphitic structures and their use for flexible and highly sensitive sensor and sensor arrays *Carbon* **96** 522–31
- [30] Zhang Y, Anderson N, Bland S, Nutt S, Jursich G and Joshi S 2017 All-printed strain sensors: Building blocks of the aircraft structural health monitoring system *Sensors Actuators A* **253** 165–72
- [31] Laflamme S, Kolloche M, Connor J J and Kofod G 2013 Robust flexible capacitive surface sensor for structural health monitoring applications *J. Eng. Mech.* **139** 879–85
- [32] Downey A, Laflamme S and Ubertini F 2017 Durability assessment of soft elastomeric capacitor skin for shm of wind turbine blades *Nondestructive Characterization and Monitoring of Advanced Materials, Aerospace, and Civil Infrastructure 2017* ed H F Wu (SPIE) p 10599
- [33] Laflamme S, Saleem H S, Vasani B K, Geiger R L, Chen D, Kessler M R and Rajan K 2013 Soft elastomeric capacitor network for strain sensing over large surfaces *IEEE/ASME Trans. Mechatronics* **18** 1647–54
- [34] Laflamme S, Ubertini F, Saleem H, D'Alessandro A, Downey A, Ceylan H and Materazzi A L 2015 Dynamic characterization of a soft elastomeric capacitor for structural health monitoring *J. Struct. Eng.* **141** 04014186
- [35] Sadoughi M, Downey A, Yan J, Hu C and Laflamme S 2018 Reconstruction of unidirectional strain maps via iterative signal fusion for mesoscale structures monitored by a sensing skin *Mech. Syst. Signal Process.* **112** 401–16
- [36] Downey A, Laflamme S and Ubertini F 2016 Reconstruction of in-plane strain maps using hybrid dense sensor network composed of sensing skin *Meas. Sci. Technol.* **27** 124016
- [37] Kong X, Li J, Collins W, Bennett C, Laflamme S and Jo H 2017 A large-area strain sensing technology for monitoring fatigue cracks in steel bridges *Smart Mater. Struct.* **26** 085024
- [38] Laflamme S, Cao L, Chatzi E and Ubertini F 2016 Damage detection and localization from dense network of strain sensors *Shock Vib.* **2016** 1–13
- [39] Downey A, Laflamme S and Ubertini F 2017 Experimental wind tunnel study of a smart sensing skin for condition evaluation of a wind turbine blade *Smart Mater. Struct.* **26** 125005
- [40] Park J and Sandberg I W 1991 universal approximation using radial-basis-function networks *Neural Comput.* **3** 246–57
- [41] De Boor C 1978 *A Practical Guide to Splines* vol 27 (New York: Springer) Etats-Unis Mathématicien
- [42] Rasmussen C E 2004 *Gaussian Processes in Machine Learning* (Berlin: Springer) (https://doi.org/10.1007/978-3-540-28650-9_4)
- [43] Day R E 1990 The role of titanium dioxide pigments in the degradation and stabilisation of polymers in the plastics industry *Polym. Degrad. Stab.* **29** 73–92
- [44] Saleem H, Thunga M, Kolloche M, Kessler M R and Laflamme S 2014 Interfacial treatment effects on behavior of soft nano-composites for highly stretchable dielectrics *Polymer* **55** 4531–7
- [45] Dannenberg E M, Paquin L and Gwinnell H 2000 Carbon black *Kirk-Othmer Encyclopedia of Chemical Technology* (New York: Wiley) (<https://doi.org/10.1002/0471238961.0301180204011414.a01>)
- [46] Wilkinson A N, Clemens M L and Harding V M 2004 The effects of SEBS-g-maleic anhydride reaction on the morphology and properties of polypropylene/PA6/SEBS ternary blends *Polymer* **45** 5239–49
- [47] Shahriari B, Swersky K, Wang Z, Adams R P and de Freitas N 2016 Taking the human out of the loop: a review of bayesian optimization *Proc. IEEE* **104** 148–75
- [48] Hengl T, Heuvelink G B M and Stein A 2004 A generic framework for spatial prediction of soil variables based on regression-kriging *Geoderma* **120** 75–93
- [49] Tonkin M J and Larson S P 2002 Kriging water levels with a regional-linear and point-logarithmic drift *Ground Water* **40** 185–93
- [50] Kitanidis P K 1997 *Introduction to Geostatistics: Applications in Hydrogeology* (Cambridge: Cambridge University Press)
- [51] Oliver M A and Webster R 2014 A tutorial guide to geostatistics: computing and modelling variograms and kriging *CATENA* **113** 56–69
- [52] GitHub 2018 Pykrige: Kriging toolkit for python <https://github.com/bsmurphy/PyKrige>
- [53] Hibbit D, Karlsson B and Sorensen P 2007 ABAQUS/StandardAnalysis User's Manual <https://sharcnet.ca/Software/Abaqus/6.14.2/v6.14/books/usb/default.htm?startat=pt09ch38s01.html>